Journal of Materials Chemistry A

Microwave-assisted solvothermal synthesis of $LiV_yM_{1-y}OPO_4$ (M = Mn, Cr, Ti, Zr, Nb, Mo, W) cathode materials for lithium-ion batteries

Journal:	*Journal of Materials Chemistry A*
Manuscript ID	TA-ART-12-2020-011704.R1
Article Type:	Paper
Date Submitted by the Author:	31-Jan-2021
Complete List of Authors:	Kaplan, Carol; Binghamton University, Chemistry Hidalgo, Marc F.; Binghamton University, Materials Science and Engineering Zuba, Mateusz; Binghamton University, Physics, Applied Physics and Astronomy Chernova, Natasha; Binghamton University, Piper, Louis; Binghamton University, State University of New York, Department of Physics, Applied Physics, and Astronomy Whittingham, M.; Binghamton University, NECCES

ARTICLE

Microwave-assisted solvothermal synthesis of $LiV_yM_{1-y}OPO_4$ (M = Mn, Cr, Ti, Zr, Nb, Mo, W) cathode materials for lithium-ion batteries

Received 00th January 20xx,
Accepted 00th January 20xx

DOI: 10.1039/x0xx00000x

Carol Kaplan,[a] Marc Francis V. Hidalgo,[a] Mateusz J. Zuba,[b] Natasha A. Chernova,[a] Louis F. J. Piper,[bc] M. Stanley Whittingham *[a]

$LiVOPO_4$ (LVP) is a promising next generation multi-electron material with a theoretical capacity of 305 mAh/g, higher than any commercially used cathode material. LVP still faces significant commercialization challenges, including difficulty obtaining full theoretical capacity at fast rates and capacity fading over several cycles. In this paper, we show that a low temperature microwave-assisted solvothermal synthesis yields a pure LVP material that can achieve high capacity at fast rates with decent cycle stability. There is, however, evidence of side reactions occurring during cycling starting at 4.1 V that leads to a slight degradation of capacity over time. In this paper, we also compare the effects of different substituents on the electrochemical performance of LVP. Structurally, we show the 5% Nb-substituted material adopts the beta phase, and the Ti-substituted LVP exhibits roughly 50/50 epsilon/beta phase, while all other substituents tend towards the epsilon phase. Ti-, Nb-, and Mo- substitution noticeably improved the electrochemical performance, while the other substituents either worsened or did not affect the material's electrochemical performance.

Introduction

The need for better, safer lithium-ion batteries is steadily climbing due to global efforts to offset carbon-based fuel sources with renewable energies for grid storage and electric vehicle applications. While layered oxides and olivines currently dominate the market, there are inherent drawbacks to each of them. Layered oxides can be thermally unstable, releasing oxygen leading to electrolyte combustion. Olivines, while much safer, provide limited energy density.[1] Currently, there is significant interest in battery cathodes that can cycle more than one lithium per redox center, effectively doubling the energy density of current commercially used cathodes.[1,2] Vanadyl phosphates are one such cathode material that cycle two lithium ions per vanadium through the formation of $VOPO_4 \leftrightarrow LiVOPO_4 \leftrightarrow Li_2VOPO_4$ during cycling.[3] The V^{5+}/V^{4+} and V^{4+}/V^{3+} redox couples are at 4.0 V and 2.5 V, respectively, which are both in the stable voltage window for current commercially available electrolytes. This high voltage and multi-electron cycling results in a high theoretical capacity of 305 mAh/g and specific energy over 900 Wh/g.[4,5] The poor kinetics associated with the large particle size of the (Li)$VOPO_4$ is a key hurdle restricting it from being commercially ready.

Low-temperature synthesis methods are one way to decrease the particle size, which may influence the kinetic limitations. Siu *et al.* obtained a nanosized $VOPO_4$ material that achieved good capacity retention at slow rates[6], however, $LiVOPO_4$ might be a better option for full cells as it already has lithium in the system. Many different synthesis methods have been utilized to obtain $LiVOPO_4$, including hydrothermal[4,7–11], solid-state[12–14], sol-gel[15–21], and microwave[22] synthesis methods. Chung *et al.* achieved theoretical capacity with hydrothermally synthesized LVP, but the capacity faded quickly, reducing to 160 mAh/g after just 20 cycles at a rate of C/20 (C = 1 Li).[7] A material with better cycle stability must be obtained. Microwave synthesis is an alternative to hydrothermal synthesis due to its shorter reaction time at a low temperature. The shorter synthesis time might alleviate particle aggregation during heating leading to smaller particles with better cycle stability. Microwave-assisted methods have been used in conjunction with other methods such as sol-gel and hydrothermal. A study by Harrison *et al.* developed a microwave-assisted hydrothermal technique to create the three most common polymorphs of $LiVOPO_4$; however, theoretical capacity was still not achieved.[22]

Another way to improve this material's kinetics and cycle stability is to substitute the vanadium in $LiVOPO_4$ with other transition metals. The key to successful substitution, as both Omenya *et al.* and Harrison *et al.* point out in the $LiFePO_4$ system – a model material for the LVP system – is reaction temperature.[23–26] Although there have been several reports on low temperature transition metal substitution in $LiVOPO_4$, they all focus on intercalating only one Li-ion into the structure.[27–30] Wen *et al.*, however, reports successful substitution of molybdenum into ε-$VOPO_4$ which improves the kinetics and capacity of the material over the full two lithium electrochemical window.[5]

In this study, a microwave-assisted solvothermal synthesis technique – similar to the one used by Harrison *et. al.*[22] – was adopted to synthesize pristine ε-$LiVOPO_4$ (ε-LVP) that reaches theoretical capacity with good cycle stability when cycled at a rate of C/10 (C = 1 Li) or slower. This synthesis was repeated with 5% Ti, Cr, Mn, Zr, Nb, Mo, and W substituted for the vanadium to determine how the transition metals affected the electrochemical performance of $LiVOPO_4$. A substitution ratio of 5% substituent to 95% vanadium was chosen based on previous work our group has done[5], indicating 5% to be the maximum

[a] NECCES, Binghamton University, Binghamton, NY 13902, USA. Email: stanwhit@gmail.com
[b] Materials Science and Engineering, Binghamton University, Binghamton, NY 13902, USA
[c] Physics Department, Binghamton University, Binghamton, NY 13902, USA
Electronic Supplementary Information (ESI) available: See DOI: 10.1039/x0xx00000x

amount that will not negatively affect the material's performance.

Experimental

Synthesis of substituted $LiV_yM_{1-y}OPO_4$

$LiV_yM_{1-y}OPO_4$ (M = Mn, Cr, Ti, Zr, Nb, Mo, W, y = 0.05) was synthesized using a microwave-assisted hydrothermal method. Stoichiometric amounts of vanadium (V) oxide (Sigma-Aldrich), oxalic acid (Sigma-Aldrich), and transition metal salt (5% of ammonium niobate (V) oxalate hydrate (Sigma-Aldrich), manganese (II) nitrate tetrahydrate (Sigma-Aldrich), ammonium molybdate (Alfa Aesar), chromium (III) acetate hydroxide (Aldrich), zirconium (IV) isopropoxide isopropanol complex (Sigma-Aldrich), ammonium titanyl oxalate monohydrate (Fisher), and ammonium metatungstate hydrate (Aldrich)) were mixed with excess phosphoric acid (J.T. Baker) in a 3:1 volume ratio of distilled water and ethanol. The color of the solution turned from mustard yellow to dark green. After 18 hours, a stoichiometric amount of lithium hydroxide monohydrate (Sigma-Aldrich) was dissolved for an additional 4 hours. An even distribution of the slurry was transferred to 4 quartz microwave vessels with stir bars and microwaved at 280 °C and 65 bar for 30 minutes using an Anton Paar Microwave Reaction System SLOV Multiwave PRO with Rotor 8N and NXQ80 vessels. The resulting powder (1 g yield) was collected, washed, and dried at 60 °C. The powder's color ranged from green to red to brown, depending on the transition metal additive.

Materials characterization

Powder X-ray diffraction (XRD) patterns were collected by a Bruker D8 Advance diffractometer with filtered Cu Kα radiation. ICDD-PDF numbers 04-012-5314 and 00-047-0469 were used as references for ε-$LiVOPO_4$ and β-$LiVOPO_4$, respectively, during refinement analysis. Scanning electron microscopy (SEM) was used to study the morphology and particle size by the Zeiss Supra-55 VP field emission scanning electron microscope. The elemental composition was confirmed by inductively coupled plasma optical emission spectroscopy (ICP-OES) using Varian Vista-MPX Axial. 3-5 mg of analyte was dissolved in a 3:1 volume ratio of nitric acid and hydrochloric acid. Afterward, the acid mixture was diluted to 50 mL with distilled water. Carbon hydrogen nitrogen sulfur (CHNS) analysis was conducted at Atlantic Microlab, Inc. for accurate proton analysis. Thermogravimetric analysis with mass spectrometry (TGA-MS) was performed using a Perkin Elmer TGA 7 under flowing oxygen or nitrogen at a heating rate of 5 °C/min up to 600 °C. Magnetic properties were measured with a superconducting quantum interference device (SQUID) magnetometer, Quantum Design MPMS XL SQUID. The temperature dependences of the DC magnetization were measuring upon cooling the samples from 350 K to 2 K in a magnetic field of 1000 Oe. X-ray absorption spectroscopy (XAS) data was collected in transmission mode at the V (5.465 keV) K-edge at the Advanced Photon Source (APS), Argonne National Laboratory, beamline 20-BM and in fluorescence mode at the Cr (5.989 keV), Mn (6.539 keV), Nb (18.986 keV), Mo (20.000 keV) K-edges at the National Synchrotron Light Source II (NSLS II), Brookhaven National Lab, beamline 6BM.

Electrochemical characterization

Electrodes were made by high energy ball milling (HEBM), the active material with graphene nanoplatelets (XG Sciences, 750 m^2/g) as the conductive additive. The ball-milled powder was hand mixed with polyvinylidene fluoride (PVDF) and 1-methyl-2-pyrrolidinone (NMP). The ratio of active material to graphene additive to PVDF was 75:15:10. The slurry was cast onto a carbon-coated aluminum foil resulting in electrodes with an area of 1.2 cm^2. Electrodes were assembled versus lithium into coin cells in an argon-filled glove box using 1M $LiPF_6$ in a 1:1 volume ratio of ethylene carbonate (EC): dimethyl carbonate (DMC) as the electrolyte. Galvanostatic charge-discharge tests were conducted using a voltage window of 1.5 V – 4.5 V and a current density of C/10 and C/20 where C = 1 Li, or 159 mAh/g. Cyclic voltammetry was used with a sweeping rate of of 0.4 mV/s, 0.2 mV/s, 0.1 mV/s, and 0.05 mV/s. Diffusion coefficient calculations were done using the equation:

$$i_p = (2.69x10^5)n^{\frac{3}{2}}AD^{\frac{1}{2}}Cv^{\frac{1}{2}}$$

Where $i_p$is the current, n is the number of electrons, A is the area of the electrode, D is the diffusion coefficient, C is the Li-ion concentration, and v is the scan frequency. The lithium concentration that was used was 0.019757 mol/cm^3 for β-$LiVOPO_4$ and 0.019419 mol/cm^3 for ε-$LiVOPO_4$.

Results and Discussion

Characterization of microwave synthesized pristine $LiVOPO_4$

Pristine $LiVOPO_4$ (LVP) was synthesized via microwave-assisted hydrothermal synthesis. ICP indicates a formula of $Li_{1.10}V_{0.97}OPO_4$. In the experimental XRD pattern (Fig. 1), the epsilon phase is clearly the dominant phase, however, small beta peaks are clearly present. According to Rietveld refinement, 98 % of the material is ε-$LiVOPO_4$, while the other 2 % is β-$LiVOPO_4$ resulting in a low R_{wp} of 5.35 %. The lattice parameters of the ε-$LiVOPO_4$ are a = 6.78(1) Å, b = 7.22(1) Å, c = 7.90(1) Å, and V = 343.7 $Å^3$, similar to the literature values of a = 6.75 Å, b = 7.21 Å, c = 7.92 Å, and V = 343.2 $Å^3$.[31] The volume is slightly larger than the theoretical value indicating the potential presence of non-stoichiometry and/or additional species, such as protons or structural water.

TGA-MS shows a slight weight loss (0.9 %) detected as water and hydroxide starting at 300 °C when the sample is heated in an oxygen atmosphere (**Error! Reference source not found.**a). 1.5 mol H or 0.09

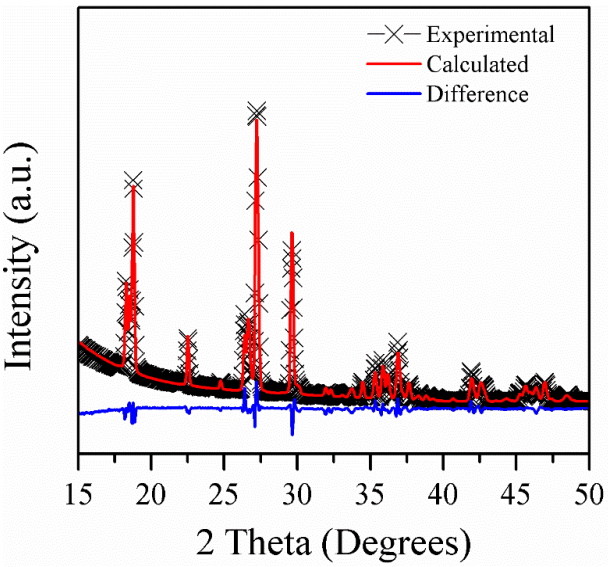

Fig. 1. XRD of microwave $LiVOPO_4$ indicates 98% ε-$LiVOPO_4$ and 2% β-$LiVOPO_4$ with no other impurities.

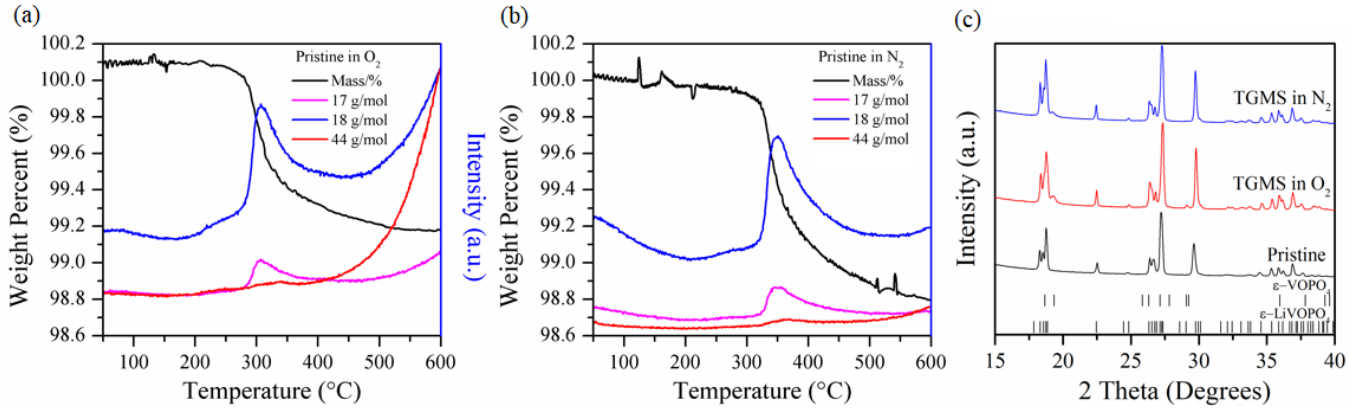

Figure 2. TGA-MS of pristine $LiVOPO_4$ in (a) oxygen and (b) nitrogen with mass spectrum peaks corresponding to hydroxide (magenta, 17 g/mol), water (blue, 18 g/mol), and carbon dioxide (red, 44 g/mol). (c) XRD of pristine $LiVOPO_4$ before and after TGA-MS heating in oxygen and nitrogen atmospheres.

mol H_2O can be calculated from a 0.9 % weight loss assuming the weight loss is from either protons or water, respectively. When run in an inert (N_2) atmosphere, the weight loss goes up slightly to 1.1 %, giving off a water signal starting at roughly 350 °C (**Error! Reference source not found.**b). 0.21 mol H or 0.10 mol H_2O can be calculated from the 1.1 % weight loss assuming the protons take oxygen from the structure to leave as water. A small amount of carbon dioxide is emitted at roughly 350 °C in both atmospheres. While this will slightly decrease the number of calculated protons, the amount of carbon dioxide produced will not significantly contribute to the weight loss seen. Both XRDs taken after TGA-MS heating in oxygen and nitrogen (**Error! Reference source not found.**c) show mainly ε-$LiVOPO_4$ with signs that ε-$VOPO_4$ formed during heating.

Carbon, hydrogen, nitrogen, and sulfur (CHNS) analysis indicates there is 0.18 mol of H in the material. This technique does not differentiate where the hydrogens come from but does match closely to the calculated amount of water from TGA-MS in both atmospheres. CHNS does not indicate carbon present in the sample, confirming the amount of carbon dioxide seen via the MS signal does not affect the calculated number of protons.

According to the linear combination fitting of V K-edge XAS measurements, there is 98 % V^{4+} with 2 % V^{3+} in the pristine LVP. Magnetic properties indicate the sample's effective magnetic moment is 1.76 μ_B ± 0.10 μ_B normalized by the transition metal amount detected by ICP (0.97 mol V). This value is in good agreement with the calculated effective magnetic moment determined from the oxidation states measured by XAS – 1.81 μ_B – normalized by the transition metal amount detected by ICP (0.97 mol V). For theoretical calculations, the spin contribution of V^{4+} (d^1, S = ½) and V^{3+} (d^2, S = 1) were considered.

Assuming the vanadium is reduced due to the presence of protons, we can extract that there is 0.02 mol of H/P based on the $Li_{1.1}V_{0.97}OPO_4$ structure. According to CHNS, this leaves 0.16 mol of H/P left unaccounted for that does not influence the vanadium oxidation state. If the unaccounted-for hydrogen is in the form of water, we would expect to see a 0.9 % weight loss in TGA-MS in an oxygen atmosphere. In a nitrogen atmosphere, where the protons grab structural oxygen before leaving, we expect to see a 1.0 % weight loss. Both are in good agreement with the experimental TGA-MS results. Therefore, the updated elemental ratio of the pristine LVP is $H_{0.02}Li_{1.1}V_{0.97}OPO_4 \cdot 0.08H_2O$.

For this highly insulating material, crystal size is a key parameter for better electrochemistry. Previous work done by our group suggests that small particle size is advantageous for better capacity and longer cycle life of vanadyl phosphates-based cathodes.[6,13,32] Microwave synthesized pristine LVP crystals are 2-4 µm crystals generally aggregate into larger clusters, as seen in Fig. 3a. These large particles were high energy ball-milled (HEBM) with 15 % graphene during electrode preparation to reduce the particle size as well as to coat the material in conductive carbon. Fig. 3b shows the reduction in particle size after ball milling and the destruction of the original morphology. XRD done before and after HEBM (Fig. 3c samples [1] and [3], respectively) shows a loss of crystallinity after ball milling. Our group's previous work on solid-state synthesized LVP shows the degradation of the crystals after HEBM is detrimental to the long-term cycling of the material. However, a post anneal step done after HEBM can be used to regain some crystallinity and enhance the cycle life of the material.[13] Four different electrode preparation methods, seen in Table 1, were examined to determine if HEBM and or annealing were necessary for this material.

The XRD comparison of samples [1 - 4] is found in Fig. 3c. Samples [1] and [2] – the hand-milled samples – have narrower-width peaks compared to samples [3] and [4] – the HEBM samples – indicative of their larger particle size. This is consistent with the SEM images seen in Fig. 3a and b. There is a decrease in peak intensity after heating the microwave samples, contrasting what was found in the solid-state samples. Sample [1] has the highest peak intensities, which correspond to the most crystalline sample. After post anneal, the crystallinity goes down (sample [2]). Similarly, crystallinity decreases between samples [3] and [4], although much less noticeable because the HEBM already breaks apart the crystal lattice showing a reduction in crystallinity and particle size. The possible presence of protons and water in the microwave samples may degrade the crystal lattice permanently as these species leave upon heating.

Cells [1] – [4] were cycled at a rate of C/10 (C = 1 Li, roughly 0.40 mA/cm^2). The first full cycle of each can be seen in Fig. 3d; the

Table 1. Pristine LVP electrode sample preparation and the corresponding coulombic efficiency based on the first cycle. The anneal step came before the hand-milling step, but after the high energy ball milling step.

Sample Name	Milling	Milling time	Anneal	Coulombic Efficiency
[1]	Hand Milled	1 h	None	86.1%
[2]	Hand Milled	1 h	450 °C, 12 h	85.9%
[3]	HEBM	0.5 h	None	92.8%
[4]	HEBM	0.5 h	450 °C, 12 h	92.7%

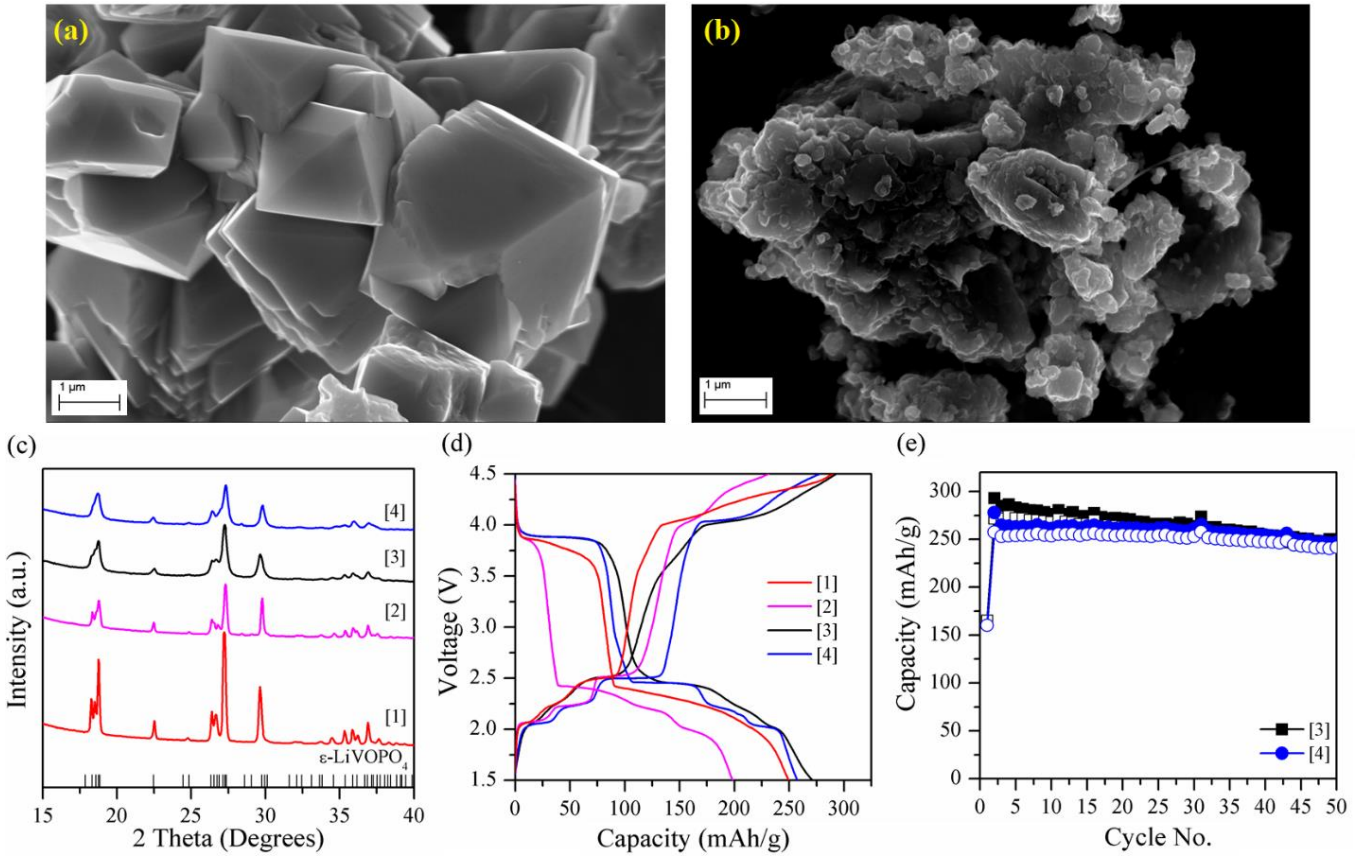

Fig. 3. Pristine $LiVOPO_4$ powder compared before (a) and after (b) high energy ball milling with graphene. Electrodes outlined in **Error! Reference source not found.** compared via (c) XRD, (d) first cycle galvanostatic charge-discharge, and (e) cycle stability. Both electrochemical tests (d) and (e), were run at a rate of C/10 (where C = 1 Li, or roughly 0.40 mA/cm^2).

coulombic efficiencies of the first cycle are seen in Table 1. The HEBM samples ([3] and [4]) have much better first cycle capacity as well as higher coulombic efficiency than the HM samples ([1] and [2]). This is most likely due to the smaller particle size achieved by HEBM since the post anneal did not affect the coulombic efficiency. Smaller particles give higher capacity, especially in the high voltage region, seen here in Fig. 3d, which is where the change in capacity upon discharge mostly comes from.

The high voltage plateau shows not only better capacity for the HEBM samples ([3] and [4]) but also a better capacity for the non-annealed samples ([1] and [3]) compared to the annealed samples ([2] and [4]). Samples [1] and [3] have a longer high voltage plateau upon discharge than their annealed analogs. In the low voltage region, characteristic steps of the epsilon $LiVOPO_4$ phase emerge more after the samples were annealed (samples [2] and [4]). Since the crystallinity decreases with annealing, the steps are likely associated with the lack of protons.

There is a slight change in slope present upon charging in samples [1] and [3] at 3.5 V that is not present in the annealed samples. This could be due to the presence of protons, or a small structural phase that is not present in the post-annealed sample. It is possible the plateau gets washed out upon discharge, similar to the voltage steps in the low voltage region. This feature is absent initially in the post heated samples, however, emerges upon long-term cycling of sample [3] The emergence of this feature suggests either protons from electrolyte decomposition will eventually cycle in the material, or the structural phase not originally present in the heated samples begins to form over time. It is well known that VPO compounds are good oxidation catalysts, so it is expected that there will be some electrolyte decomposition.[33] While we do see a steady decline in the non-annealed sample [3], Fig. 3e, sample [4] shows a more stable cycle life even with the emergence of the feature at 3.5 V on later cycles. This might point more towards a small structural phase impurity than electrolyte decomposition.

To further investigate the effects of HEBM versus HM, XAS measurements were taken on samples [1] – [4] (Fig. 4). First, we look at the consequences of electrode preparation overall as we compare the powder to its electrode analog. The oxidation state in all samples shows majority V^{4+}, which is expected in the $LiVOPO_4$ system. It is evident, however, that some reduction occurs during slurry preparation as the vanadium pre-edge peak loses intensity slightly for the electrode samples [1] and [2]. The HEBM samples ([3] and [4]) are more reduced than the HM samples ([1] and [2]), which is consistent with what has been previously reported.[6] It is likely that the vanadium gets reduced during the HEBM step, probably due to a combination of heat and carbon reduction. No change was seen in the vanadium's oxidation state before and after the HEBM samples were made into electrodes.

It can be concluded that hand milling shows no advantage over HEBM samples during electrode preparation, indicating that the particle size needs to be reduced to enhance electrochemical performance. While heating has adverse effects on the first cycle capacity, it improves the long-term cycle stability (Fig. 3e). After roughly 30 cycles, sample [4] has a higher capacity than sample [3] with minimal capacity fade.

Capacity fade is associated with parasitic side reactions in most cases. As the cell reaches 4.5 V, electrolyte decomposition is more plausible, which can lead to surface species and electrolyte loss. In

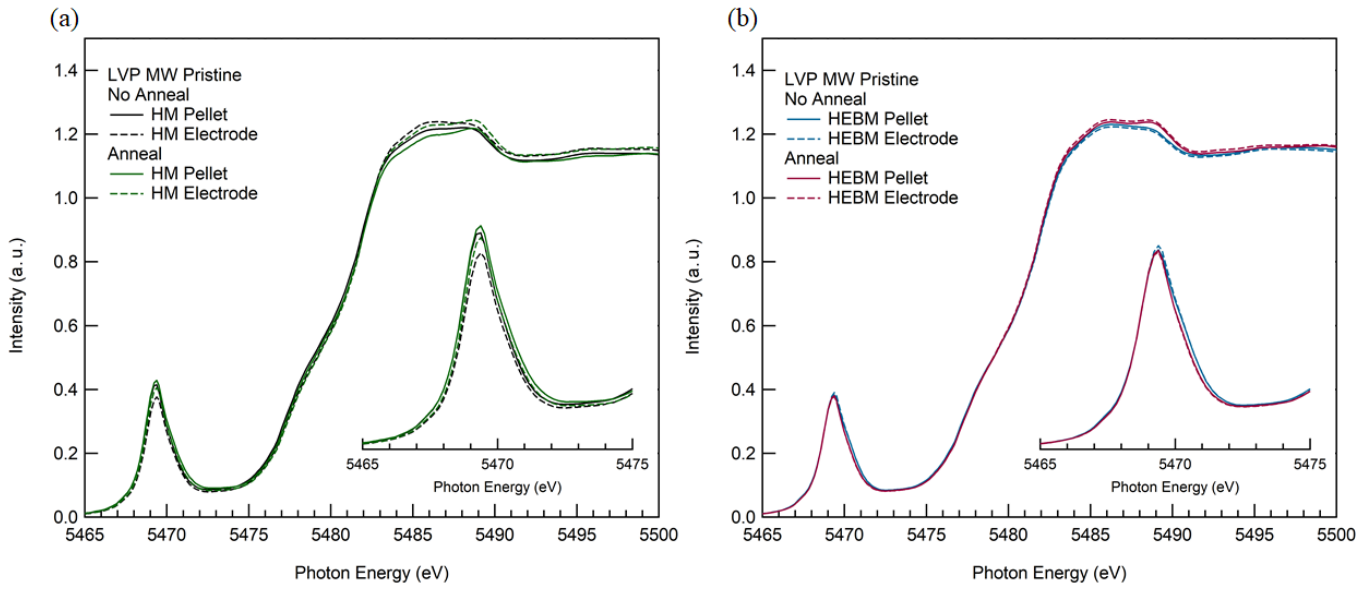

Fig. 4. XANES of vanadium edge for pristine samples that were (a) hand mixed and (b) high energy ball milled when preparing electrodes.

the LVP system upon charging, there is a tail-like feature that changes shape between the annealed and non-annealed samples, which is likely indicative of side reactions. Samples [2] and [4] have sharper slopes in the 4.1 V – 4.5 V tail-like region (Fig. 3d), which does not seem to affect the first cycle capacity, however, this may indicate a difference in side reaction activity within that region. To better understand this tail-like feature, different electrochemical testing methods were performed on the HEBM sample with no anneal (sample [3]). The three different methods used were (a) discharge to 1.5 V then charge to 4.5 V (b) charge to 4.5 V then discharge to 1.5 V and (c) discharge to 1.5 V then charge to 4.1 V. The initial charge or discharge along with the first and fifth full cycle for each method is shown in Fig. 5. The initial charge or discharge in Fig. 5a and b have similar capacities indicating that protons do not initially get extracted from the pristine material. The slope of the first tail upon charging first to 4.5 V changes after the initial charge seen in Fig. 5b. This likely indicates a change in the reaction mechanism after the initial charge. When the voltage is cut off before the appearance of the tail-like feature, Fig. 5c, the coulombic efficiency increases; however, the capacity unsurprisingly decreases (the vanadium is not allowed to fully oxidize to V^{5+}). The tail seems to contribute to the poor coulombic efficiency seen in both Fig. 5a and b suggesting side reactions are occurring between 4.1 V and 4.5 V. We know from previous work that protons can be removed from H_2VOPO_4 at some voltage, so it follows that at least some of this feature is due to proton removal.[3]

To further understand the side reactions occurring during cycling, samples [3] and [4] were studied more closely with ex-situ XAS measurements done at the initial charge state (OCV), 4.1 V, 4.5 V, and 1.5 V (Fig. 6). Cells were first discharged to 1.5 V, then charged to 4.1 V, 4.5 V, and finally discharged again to 1.5 V and held for 5 hours at each charge state endpoint to allow for equilibration. The linear fit of the pre-edge region yielded V^{3+}, V^{4+}, and V^{5+} percentages, given in Table 3 for each of the samples. At OCV, it is expected that since the material is $LiVOPO_4$, the vanadium will be all V^{4+}. However, as previously discussed, there are not only protons in the structure that will contribute to the presence of V^{3+}, but the HEBM process itself will reduce the vanadium due to a combination of heat and carbon reduction.

Upon charging to 4.1 V, before the tail seen during charging, there is mostly V^{4+} present with some V^{5+} in both the annealed and non-annealed samples. For the annealed sample, the calculated number of lithium-ions based on the capacity at this point (213 mAh/g) and the oxidation state of the vanadium do not agree for

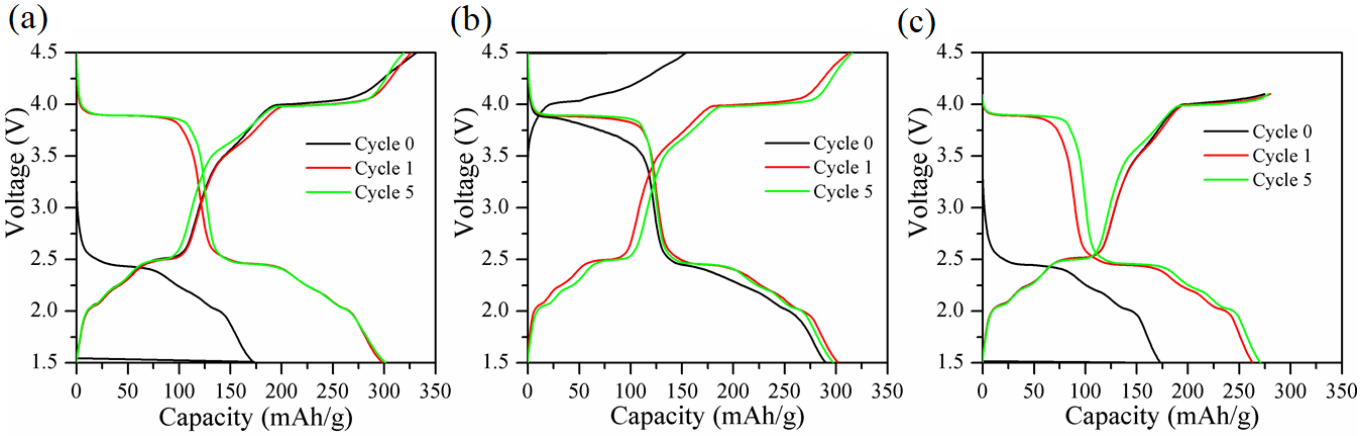

Fig. 5. $LiVOPO_4$ cycled (a) at a rate of C/20 (C = 1 Li, or 0.30 mA/cm^2) first discharged then charged with a voltage window of 1.5V – 4.5V (b) at a rate of C/20 (C = 1 Li, or 0.28 mA/cm^2)first charged then discharge with a voltage window of 1.5 V – 4.5 V and (c) at a rate of C/20 (C = 1 Li, or 0.61 mA/cm^2) first discharged then charged with a voltage window of 1.5 V – 4.1 V.

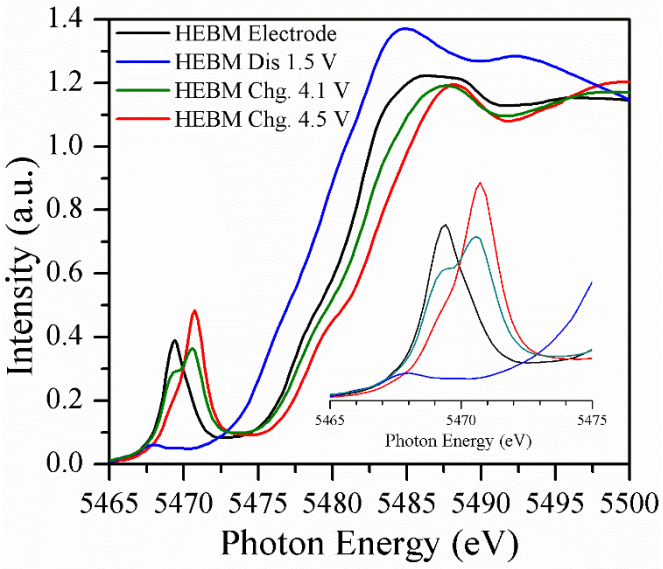

Fig. 6. Ex-situ XANES measurements of pristine LVP cycled to 1.5 V, 4.1 V, and 4.5 V to show the evolution of the vanadium oxidation state upon cycling.

either cell. Based on oxidation states for the vanadium, there should be 0.88 mol of Li left in the LVP structure, but electrochemical data implies there is roughly 0.67 mol of Li left at 4.1 V. This implies that there is roughly 33 mAh/g of extra capacity that does not come from lithium intercalation. As for the non-annealed sample, the electrochemical data and the vanadium oxidation states are in better agreement – 0.58 mol of Li versus 0.63 mol of Li, respectively – showing only an 8 mAh/g difference in capacity. At this point it is already clear that the annealed sample may promote more side reactions than the non-annealed sample.

The most significant evidence of side reactions comes during charging from 4.1 V to 4.5 V. The amount of capacity obtained from charging sample [3] to 4.5 V (310 mAh/g) indicates two full lithium-ions were pulled from the structure. The percentage of V^{5+}, however, indicates that 0.33 Li is still in the structure. For sample [4], the capacity obtained electrochemically (278 mAh/g) indicates 0.25 Li still in the structure, while vanadium oxidation states indicate 0.60 Li are left, almost twice what was seen from sample [3]. While this difference in lithium content can be attributed to side reactions, there is a stark difference between the reactivity of the two samples. As mentioned previously, this voltage region looks different between the two samples, which may indicate different reactions occur within the cell. The sample with more protons (sample [3]) has both electrochemistry and vanadium oxidation states that suggest fewer parasitic reactions than the annealed sample [4]. Since both samples' coulombic efficiencies are the same (Table 1), some of the lithium retention could be attributed to the same kinetic limitations imposed upon the $LiVOPO_4$ system due to the increased structural distortion caused by the HEBM step.[32] However, since there seem to be more side reactions with the annealed sample, it suggests the presence of protons and water are beneficial during cycling in the high voltage region.

When the sample is discharged to 1.5 V, the vanadium in both samples [3] and [4] is nearly fully reduced to V^{3+}. This suggests that nearly two full lithium ions were inserted into the $VOPO_4$ structure upon discharge. Since there was still 0.33 and 0.60 Li left in sample [3] and [4], respectively, it is not surprising that the capacity does not reach theoretical upon discharge. There is, however, an extra bit of capacity unaccounted for in both samples. It has been shown that there is a formation of a CEI layer – most likely Li_2O from electrolyte decomposition – during the discharge process that would account for the small discrepancies in the vanadium oxidation state and capacity obtained.[32,34] While this would account for the excess capacity for the annealed sample, the non-annealed sample's capacity and vanadium oxidation state matches more closely to what is expected. This suggests, once again, that the presence of protons and water are beneficial in the low-voltage region if only to stave off the electrolyte decomposition and the CEI formation layer. This CEI layer mentioned has been shown to be unstable during charge and is therefore not present in the higher voltage range.[32,34]

Table 3. Vanadium charge states of ex-situ samples HEBM with and without a post anneal (samples [4] and [3], respectively) at the specified charge state obtained from the linear approximation of XANES. Cells were first discharged to 1.5 V, then charged to 4.1 V, 4.5 V, and finally discharged again to 1.5 V and held for 5 hours at each charge state endpoint to allow for equilibration. Cells were run at a rate of C/10 where C = 1 Li (roughly 0.60 mA/cm²).

Anneal	Charge State	V^{3+} (%)	V^{4+} (%)	V^{5+} (%)
Yes	4.5 V	0.0(0)	60.5(4)	39.5(6)
No	4.5 V	0.0(0)	33.3(3)	66.7(4)
Yes	4.1 V	0.0(0)	87.6(7)	12.4(8)
No	4.1 V	0.0(0)	62.6(6)	37.4(8)
Yes	1.5 V	98.6(3)	1.4(5)	0.0(0)
No	1.5 V	96.2(4)	3.8(5)	0.0(0)
Yes	OCV	8.0(6)	92.0(8)	0.(0)
No	OCV	5.4(3)	94.8(4)	0.(0)

Substituted $LiV_yM_{1-y}OPO_4$

In order to improve the cycling performance seen in pristine non-annealed LVP, the material was substituted with 5 % of various transition metals during synthesis to form $LiV_yM_{1-y}VOPO_4$, M = Mn, Cr, Ti, Zr, Nb, Mo, or W. Looking at the elemental ratios obtained from ICP in Table 2, it is evident that not all of the 5% transition metal went into the final product. The materials with the highest amount of substituent remaining are Nb, Ti, and Cr, with the least being Mo, W, and Zr. The XRD for each substituted LVP, seen in **Error! Reference source not found.**, shows a mixture of the triclinic (ε-) and orthorhombic (β-) $LiVOPO_4$ phases (quantifications of which shown in Table 4) with no additional impurity peaks. Mn-substituted LVP is the only sample in a pure phase, while the other substituents adopt a mixture of the ε- and β-phases. Mn, Mo, W, Cr, Zr, and the pristine

Table 2. Elemental ratios of the pristine and substituted LVP as detected by ICP measurements.

Method	ICP		
Sample	**Li/P**	**V/P**	**Substituent/P**
Pristine	1.10	0.97	-
Mn	1.01	0.94	0.03
Cr	0.99	0.90	0.04
Ti	0.80	0.83	0.04
Zr	0.87	0.96	0.01
Nb	0.74	0.94	0.04
Mo	1.00	0.94	0.02
W	0.83	0.98	0.02

are >90 % epsilon, while Nb-substituted LVP is 94 % beta. Ti-substituted LVP is roughly 50 % epsilon and beta LVP.

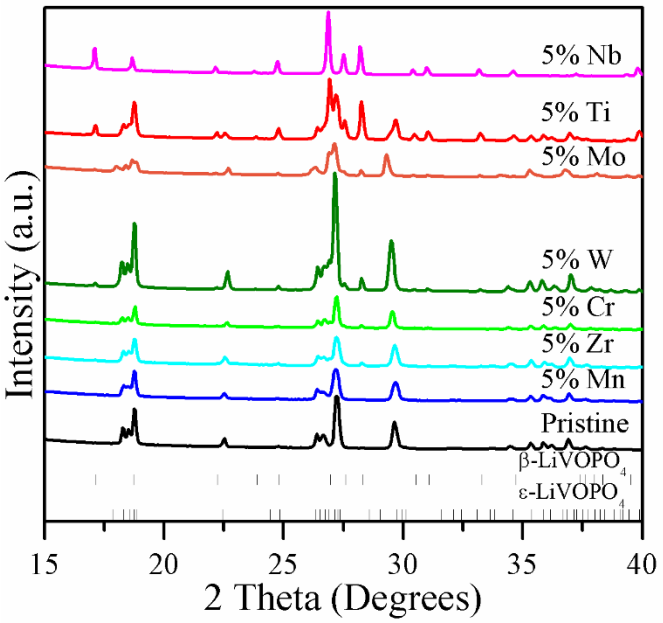

Fig. 7. XRD comparison between pristine LVP and substituted LVP.

The oxidation states of the transition metals were obtained through both XANES and magnetic data, seen here in Table 5. The oxidation states of Ti, Zr, and W were not measured via XANES, however, according to the trend the other substituents follow, the oxidation state does not change throughout the synthesis. Measured effective magnetic moments were calculated from the Curie-Weiss law fits for the temperature dependences of the magnetic susceptibility. Calculations of the effective magnetic moment take the amount of V^{3+} and the substituent oxidation state measured via XAS into account. The effective magnetic moments were normalized based on the total number of transition metals determined by ICP. The measured values match closely with the calculated values, seen in Table 5, confirming the substituent amounts determined by ICP as well as the oxidation states of Ti, Zr, and W.

According to Vegard's law, as substitution occurs, we expect to see linear lattice parameter changes that correspond to an enlargement or shrinkage of the lattice depending on the ionic radius of the substituent.[35] If the ionic radius of the substituent is larger than V^{4+}, then an increase in the lattice volume in the crystal structure is expected if successful substitution occurred. Looking at both the ε- and β-LVP lattice parameters in Table 4, the samples with Mn, Cr, W, Mo, and Ti show an increase in volume compared to the synthesized pristine $H_{0.02}Li_{1.10}V_{0.97}OPO_4 \cdot 0.08H_2O$, suggesting something was inserted into the structure. The sample containing zirconium, however, shows a very slight decrease in volume with no discernible change in the *a*, *b*, or *c* directions in the unit cell. This likely indicates that nothing was inserted into the structure. The beta phase half of the Ti sample also has a slight decrease in volume coming from a decrease in the *b* and *c* directions, but an increase in the *a* direction. It is important to remember here that the sample containing Ti is a roughly 50 % mixture of both the beta and epsilon phases. It is possible that the titanium prefers to substitute into one phase over the other, enlarging the volume of one phase (in this case, epsilon) while the other volume stays close to the pristine. Since the Nb phase is predominately in the beta phase, it's lattice parameters were compared to the beta phase's literature values. There is a slight increase in the *a*, *b*, and *c* directions and thus in the unit cell volume. Based on the evidence shown by Lee, *et. al*., Nb substitutes on the vanadium sites in the LVP structure.[36]

While an increase in the unit cell volume is a good indication that substitution occurred, it is important to remember that the presence of protons in the pristine sample, $H_{0.02}Li_{1.10}V_{0.97}OPO_4 \cdot 0.08H_2O$, influences the unit cell volume. It is likely that the substituted samples also have both protons in their structures as well, causing the increase in lattice volume rather than the substituent itself. Large volume changes from the samples with Mo, W, and Nb indicate more of a potential presence of non-stoichiometry and/or additional species, such as protons or structural water.

CHNS analysis shows an increase in the substituted samples' hydrogen content compared to the pristine, seen in Table 6. This indicates that the substituted samples contain more protonic species

Table 4. Lattice parameters of the LVP and substituted LVP.

				ε-LVP			
	Oxidation state, Ionic Radius (Å)	**a (Å)**	**b (Å)**	**c (Å)**	**V (Å³)**	**Rwp (%)**	**% of phase**
Literature[31]		6.75	7.21	7.92	343.2		
Pristine	4+, 0.58	6.78(1)	7.22(1)	7.90(1)	343.7	5.4	98.3
Mn	2+, 0.83	6.77(1)	7.24(1)	7.90(1)	344.5	5.5	100.0
Zr	4+, 0.72	6.77(3)	7.22(3)	7.89(3)	343.4	6.2	94.7
Cr	3+, 0.62	6.81(3)	7.24(3)	7.86(3)	344.2	4.7	92.5
W	6+, 0.60	6.82(3)	7.26(3)	7.86(3)	345.4	8.7	90.5
Mo	6+, 0.59	6.89(2)	7.29(2)	7.85(2)	348.7	8.4	90.2
Ti	4+, 0.61	6.78(2)	7.23(2)	7.89(2)	344.1	6.6	53.0
				β-LVP			
		a (Å)	**b (Å)**	**c (Å)**	**V (Å³)**	**Rwp (%)**	**% of phase**
Literature[8]		7.44	6.30	7.17	336.4		
Ti	4+, 0.61	7.47(1)	6.32(1)	7.19(1)	339.1	6.6	47.0
Nb	5+, 0.64	7.48(1)	6.32(1)	7.19(1)	340.1	6.4	93.8

Table 5. Oxidation states and effective magnetic moment as measured from XANES and SQUID, respectively.

	Pristine	Mn	Cr	Ti	Zr	Nb	W	Mo
Measured μ_{eff}	1.76	2.18	2.10	1.98	1.76	1.70	1.88	2.29
Substituent oxidation state		2+	3+	4+	4+	5+	6+	6+
V^{4+} % (±1 %)	98	96	96	97	94	98	91	62
V^{3+} % (±1 %)	2	4	4	3	6	3	9	38
Calculated μ_{eff}	1.81	2.10	2.05	1.99	1.85	1.76	1.81	2.28

in the structure. To differentiate the presence of water versus protons, both TGA-MS and XAS were used. TGA-MS was performed in both an oxygen and nitrogen atmosphere (8). The weight loss percentage in each atmosphere, summarized in Table 6, shows each substituent has a higher percent weight loss than the pristine confirming substitution leads to an increase in the amount of protonic species in the structure. XAS measurements were used to determine the amount of V^{3+} in each of the samples, also shown in Table 6. This was used in conjunction with ICP and CHNS data to determine the approximate number of protons and water in the structure. The assumption was then used to calculate the expected weight loss in TGA-MS to compare to the experimental weight loss to determine how good the approximation was. For aliovalent substitutions, charge compensation mechanisms also must be considered. Since Nb, Mo, and W are in a higher oxidation state than vanadium, it is likely that vanadium will be reduced to maintain neutrality. It is possible, however, that lithium or oxygen vacancies, as well as proton insertion, will also occur. The substituents with oxidation state ≤ 4+ should not affect the amount of V^{3+} in the system but instead use another form of charge compensation, if necessary. The substituents with oxidation states > 4+ should increase the amount of V^{3+} in the system along with any protons present, assuming there are no other charge compensation mechanisms at play. The assumed number of the protons and water were, for the most part, in good agreement with experimental TGA-MS results indicating the substituent influences how many protons and water will be in the structure.

It is likely that Nb, Cr, Ti, W, and Mo substitute into the LVP structure based on detection by ICP, increase in unit cell volume, XANES detection, and their effective magnetic moments. There is conflicting evidence whether Mn is incorporated into the LVP structure. While an increase in lattice parameters suggests that something was successfully inserted into the structure, the larger ionic radius for Mn^{2+} compared to V^{4+} (0.83 Å vs. 0.58 Å, respectively) would make substitution difficult. More protons are present than in the pristine, which might cause the increase in unit cell volume instead of the Mn^{2+}. The larger unit cell, however, might be necessary for the large Mn^{2+} to be successfully incorporated into the lattice. ICP does detect the presence of Mn, and XANES, as well as the calculated magnetic moment, supports the presence of Mn^{2+}, but none provide evidence of where the Mn^{2+} sits inside the structure. While it can be said Mn is present, the location of the cation cannot be confirmed and is beyond the scope of this paper. It can be said with some certainty, however, that zirconium does not substitute. There should be an increase in at least one of the directions in the unit cell to accommodate the larger Zr^{4+} ion. The lack of significant change suggests no real substitution of this ion occurred. ICP and XANES indicate a small amount of Zr is present, but it is likely not incorporated into the structure.

The morphology of substituted LVP is dependent on the substituent added during synthesis. While the pristine is 2-4 µm crystallites (Fig. 8a), the substituted LVPs range from 200 nm to 5 µm in size and small rods to more spherical meatballs or peanuts in shape (Fig. 8). The materials containing W, Mn, and Ti seem to have a similar size and shape to the pristine. The Nb morphology is the smallest being only 200 nm in width and 400-500 nm in length. This could be attributed to its orthorhombic structure (beta phase) instead of the triclinic structure (epsilon phase). The substituted LVPs, except for Nb, are too large to be cycled without the HEBM step for electrode preparation. For consistency, all of them were ball milled for 0.5 hours, as was the pristine, for electrochemical comparison.

Each substituted material was cycled at a rate of roughly 0.81 mA/cm^2 (C/10 where C = 1 Li) and compared to the pristine material (Fig. 9). The first cycle, shown in Fig. 9a, shows the high capacity of the pristine material is maintained with transition metal substitution. The majority of the curves exhibit the same profile as the pristine, which is characteristic of the ε-LVP phase. From XRD, we know the Nb-LVP material is mostly β-LVP, so it is not surprising that its electrochemical profile exhibits characteristic β-LVP electrochemistry. The Ti-LVP sample exhibits both β-LVP and ε-LVP electrochemical features seen in Fig. 9a in the low voltage region

Table 6. Proton and water analysis for each sample based on XAS, CHNS, and TGA-MS data.

	CHNS	XAS	Assumptions		TGA-MS			
					Expected	Experimental	Expected	Experimental
Sample	**H (mol)**	**V^{3+} (%)**	**H^+**	**H_2O**	**O_2**	**O_2**	**N_2**	**N_2**
Pristine	0.18	2%	0.02	0.08	0.9%	0.9%	1.0%	1.1%
Mn^{2+}	0.27	4%	0.04	0.12	1.2%	1.2%	1.4%	1.8%
Cr^{3+}	0.59	4%	0.05	0.27	2.9%	2.2%	3.1%	3.2%
Ti^{4+}	0.43	3%	0.23	0.10	1.2%	1.4%	2.4%	2.4%
Zr^{4+}	0.43	6%	0.19	0.12	1.4%	1.9%	2.3%	2.6%
Nb^{5+}	0.62	3%	0.25	0.19	2.1%	2.0%	3.2%	3.0%
Mo^{6+}	1.02	38%	0.34	0.34	3.7%	1.8%	5.2%	4.0%
W^{6+}	0.64	9%	0.22	0.21	2.3%	2.0%	3.3%	2.9%

with the characteristic voltage steps that the ε-LVP phase is known for in addition to a higher voltage step closer to 2.5 V which is most likely a contribution from the β-LVP phase. All other materials exhibit discharge capacities, and in most cases, make it worse, possibly increasing the initial side reactions inside the cell. This may be a consequence of more protons that each of the substituted materials has in comparison to the pristine.

Table 8. Initial charge and subsequent discharge capacities for the various LVP materials and their calculated coulombic efficiencies. The theoretical capacity calculations were based on 2 lithium-ions and the total molecular weights based on ICP data.

Substituent	Formula weight (g/mol)	Capacity (mAh/g)			Coulombic Efficiency
		Theoretical	Initial Charge	Subsequent Discharge	
Pristine	50.94	308	310	288	92.9%
Ti	47.87	317	316	287	91.0%
Cr	52.00	310	319	287	90.1%
Mn	54.94	307	310	276	88.9%
Zr	91.22	307	300	268	89.6%
Nb	92.91	304	311	287	92.4%
Mo	95.95	307	314	284	90.5%
W	183.84	300	302	271	89.7%

only ε-LVP electrochemical profiles.

The theoretical capacity is dependent on the formula weight of the active material. As substitution into LVP occurs, the theoretical capacity will slightly change based on the weight of the transition metal and percent incorporated. The substituted materials' initial charge capacities not only closely match with the theoretical capacity values, but in some cases, exceed the expected capacity, shown in Table 7. We know from XAS data discussed previously, however, that the vanadium oxidation state in the pristine does not match the capacity obtained at 4.5 V. Therefore, it is possible that each of these samples exhibits the same type of side reactions as the pristine, which would increase the capacity obtained for each sample. The discharge capacities are slightly smaller, creating a relatively low coulombic efficiency compared to the pristine, also shown in Table 7. These coulombic efficiencies indicate that the substituted materials do not improve the initial gap between the charge and

Table 7. Calculated diffusion coefficients based on CV data. The diffusion coefficients are mass dependent as the coefficients will increase with increasing active mass, which are also listed.

High Voltage Region (V^{4+}/V^{5+} Transition)		
Sample	**Active Mass (mg)**	**D ($x10^{-12}$ cm^2/s)**
Nb	5.925	86.51
Mn	6.225	59.82
Pristine	6.375	48.91
W	6.150	45.72
Zr	6.275	32.66
Cr	5.925	22.78
Mo	6.150	20.25
Ti	6.975	4.55

Long term cycling data, shown in Fig. 9b, shows improved cycle performance for the samples containing Mo, Ti, and Nb. All three samples start with a higher initial capacity than the pristine and maintain their higher capacity after 50 cycles. The pristine shows 90

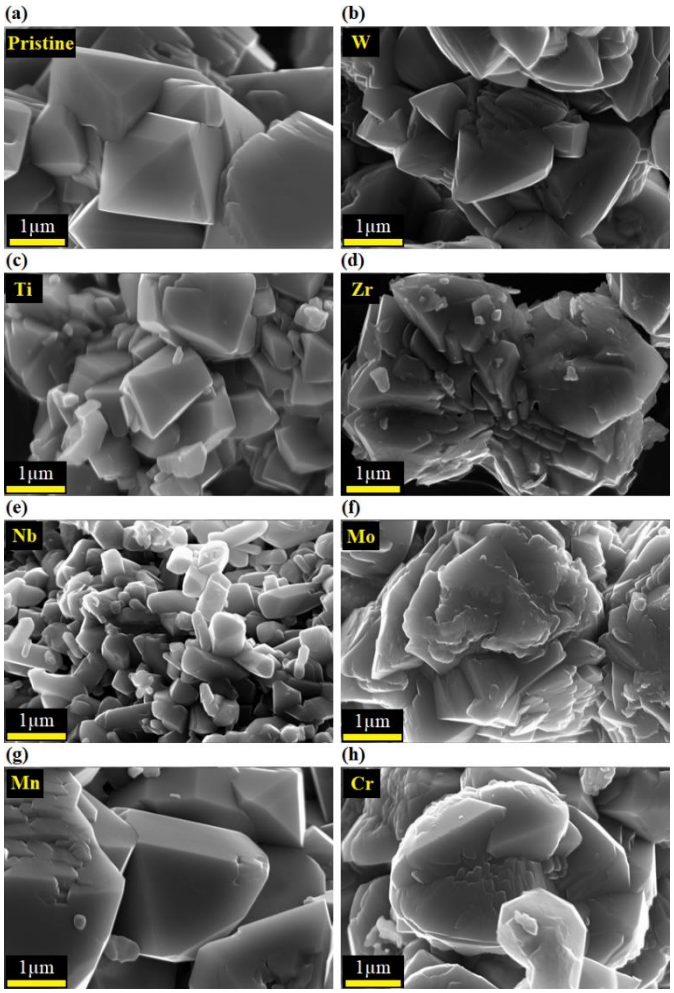

Fig. 8. SEM images of the $LiVOPO_4$ sample containing (a) Pristine (b) W (c) Ti (d) Zr (e) Nb (f) Mo, (g) Mn, and (h) Cr.

% capacity retention after 50 cycles. Mo, Cr, and Nb show capacity retentions equal to or greater than the pristine – 92 %, 92 %, and 90 %, respectively. The rest of the substituents have slightly lower capacity retentions after the 50 cycles – W with 89 %, Mn with 87 %, Zr with 85 %, and Ti with 85%. The capacity decay, similar to the pristine sample, suggests the same side reactions are occurring in these cells, most likely due to the strain HEBM induces in the system (discussed above). The samples containing W, Cr, and Mn have similar electrochemical performance as the pristine, while the sample containing Zr shows a faster capacity fade.

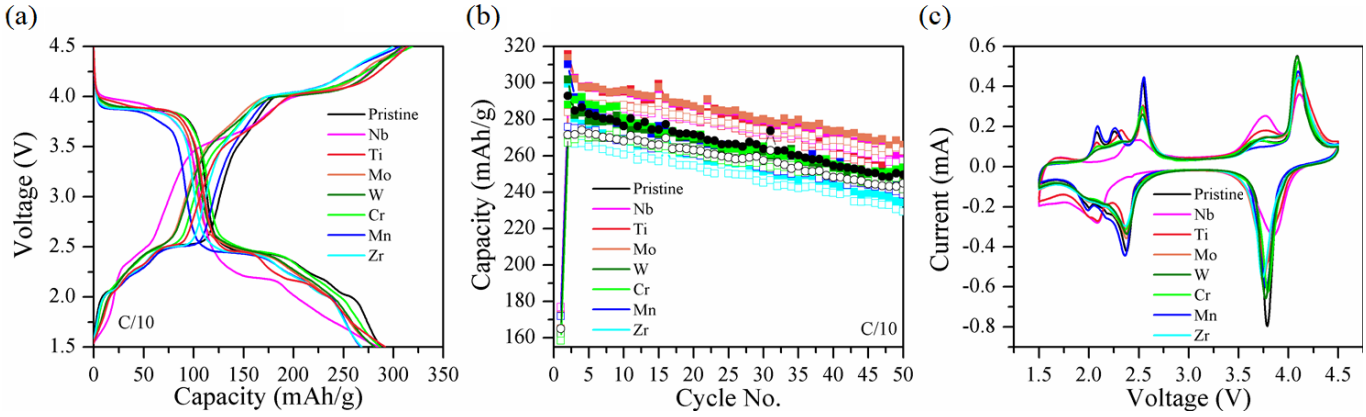

Fig. 9. Electrochemistry of substituted samples compared to the pristine. (a) First cycle galvanostatic charge/discharge curve of substituted LVP run at a rate of C/10 (C = 1 Li, or 0.81 mA/cm^2) (b) cycle stability of substituted and pristine LVP samples (c) CV study on LVP and substituted LVP.

Cyclic voltammetry of each of the materials, shown in Fig. 9c, shows no perceptible signs of change in the polarization during the first cycle of the substituted materials. From this technique, the diffusion coefficient can be calculated. The larger the diffusion coefficient is for a sample, the better kinetics the material will have. The diffusion coefficients for the V^{4+} to V^{5+} transition in each of the substituted materials are listed in Table 8. Two samples, Nb and Mn, improve the initial kinetics of the pristine sample in the upper voltage region. As mentioned previously, Nb likely substitutes into the LVP structure; however, it is unclear if Mn sits in the structure. The other samples have lower diffusion coefficients than the pristine.

Conclusions

$LiVOPO_4$ was successfully synthesized by a microwave-assisted hydrothermal method and showed theoretical capacity could be obtained with good cycle stability up to 50 cycles. An enlarged unit cell volume suggests the presence of protons or structural water, confirmed by CHNS and TGA-MS. Magnetic data combined with XANES confirm a small number of protons affect the vanadium oxidation state, but the majority of the hydrogens do not, suggesting more of a presence of water. HEBM is necessary for the material to cycle well, but post-annealing the structure suggests the protons and water are beneficial to stave off side reactions and utilize more of the vanadium redox chemistry.

The addition of substituents changes the phase of the LVP depending on which transition metal is used. While the addition of W, Zr, Mo, Mn, and Cr keep the LVP in the same epsilon phase as the pristine, the addition of Nb changes the sample to the beta phase. The addition of Ti makes the material adopt half of the beta phase and half of the epsilon phase. Successful substitution was achieved from Cr, W, Mo, Ti, and Nb substituents, however, Zr did not substitute. There is conflicting evidence of successful Mn substitution. ICP confirmed the presence of the substituent while XAS determined their oxidations states. XANES indicated the vanadium oxidation state was affected for the Mo and W substituted samples but was virtually unaffected by the other substituents with lower oxidation states. The Mo, Ti, and Nb substituted materials achieved a higher initial capacity in addition to better cycle life. All the substituted samples, including the materials with Mn and Zr present, had similar % capacity retention as the pristine. None of the substituted samples, however, achieved better coulombic efficiency or higher lithium diffusivity than the pristine during the first cycle.

Conflicts of interest

There are no conflicts to declare.

Acknowledgements

This work was supported by the NorthEast Center for Chemical Energy Storage (NECCES), an Energy Frontier Research Center funded by the U.S. Department of Energy, Office of Science, Office of Basic Energy Sciences under Award Number DE-SC0012583. This research used resources (Beamline 6BMM) of the National Synchrotron Light Source II (NSLS-II), a U.S. Department of Energy (DOE) Office of Science User Facility operated for the DOE Office of Science by Brookhaven National Laboratory under Contract No. DE- SC0012704. This research used resources (Beamline 20-BM) of the Advanced Photon Source, a U.S. Department of Energy (DOE) Office of Science User Facility operated for the DOE Office of Science by Argonne National Laboratory under Contract No. DE-AC02- 06CH11357. The authors gratefully acknowledge Drs. Bruce Ravel and Dale Brewe for their assistance during XAS measurements at NSLS II and APS, respectively.

References

1 M. S. Whittingham, *Chem. Rev.*, 2004, **104**, 4271–4301.
2 M. S. Whittingham, *Chem. Rev.*, 2014, **114**, 11414–11443.
3 Y. Song, P. Y. Zavalij and M. S. Whittingham, *J. Electrochem. Soc.*, 2005, **152**, A721.
4 M. F. V. Hidalgo, Y. C. Lin, A. Grenier, D. Xiao, J. Rana, R. Tran, H. Xin, M. Zuba, J. Donohue, F. O. Omenya, I. H. Chu, Z. Wang, X. Li, N. A. Chernova, K. W. Chapman, G. Zhou, L. Piper, S. P. Ong and M. S. Whittingham, *J. Mater. Chem. A*,

2019, **7**, 8423–8432.

5 B. Wen, Q. Wang, Y. Lin, N. A. Chernova, K. Karki, Y. Chung, F. Omenya, S. Sallis, L. F. J. Piper, S. P. Ong and M. S. Whittingham, *Chem. Mater.*, 2016, **28**, 3159–3170.

6 C. Siu, I. D. Seymour, S. Britto, H. Zhang, J. Rana, J. Feng, F. O. Omenya, H. Zhou, N. A. Chernova, G. Zhou, C. P. Grey, L. F. J. Piper and M. S. Whittingham, *Chem. Commun.*, 2018, **54**, 7802–7805.

7 Y. Chung, E. Cassidy, K. Lee, C. Siu, Y. Huang, F. Omenya, J. Rana, K. M. Wiaderek, N. A. Chernova, K. W. Chapman, L. F. J. Piper and M. S. Whittingham, *ACS Appl. Energy Mater.*, 2019, **2**, 4792–4800.

8 K. H. Lii, C. H. Li, C. Y. Cheng and S. L. Wang, *J. Solid State Chem.*, 1991, **95**, 352–359.

9 M. M. Ren, Z. Zhou, L. W. Su and X. P. Gao, *J. Power Sources*, 2009, **189**, 786–789.

10 K. Saravanan, H. S. Lee, M. Kuezma, J. J. Vittal and P. Balaya, *J. Mater. Chem.*, 2011, **21**, 10042–10050.

11 G. He, C. A. Bridges and A. Manthiram, *Chem. Mater.*, 2015, **27**, 6699–6707.

12 Y. Shi, H. Zhou, I. D. Seymour, S. Britto, J. Rana, L. W. Wangoh, Y. Huang, Q. Yin, P. J. Reeves, M. Zuba, Y. Chung, F. Omenya, N. A. Chernova, G. Zhou, L. F. J. Piper, C. P. Grey and M. S. Whittingham, *ACS Omega*, 2018, **3**, 7310–7323.

13 Y. Shi, H. Zhou, S. Britto, I. D. Seymour, K. M. Wiaderek, F. Omenya, N. A. Chernova, K. W. Chapman, C. P. Grey and M. S. Whittingham, *Electrochem. commun.*, 2019, **105**, 106491.

14 J.-M. Ateba Mba, C. Masquelier, E. Suard and L. Croguennec, *Chem. Mater.*, 2012, **24**, 1223–1234.

15 M. M. Ren, Z. Zhou and X. P. Gao, *J. Appl. Electrochem.*, 2009, **40**, 209.

16 A. P. Tang, Z. Q. He, J. Shen and G. R. Xu, *Adv. Mater. Res.*, 2012, **554**–**556**, 436–439.

17 H. Zhou, Y. Shi, F. Xin, F. Omenya and M. S. Whittingham, *ACS Appl. Mater. Interfaces*, 2017, **9**, 28537–28541.

18 C. J. Allen, Q. Jia, C. N. Chinnasamy, S. Mukerjee and K. M. Abraham, *J. Electrochem. Soc.*, 2011, **158**, A1250.

19 L. Wang, L. Yang, L. Gong, X. Jiang, K. Yuan and Z. Hu, *Electrochim. Acta*, 2011, **56**, 6906–6911.

20 B. M. Azmi, T. Ishihara, H. Nishiguchi and Y. Takita, *Electrochemistry*, 2003, **71**, 1108–1110.

21 H. T. Kuo, N. C. Bagkar, R. S. Liu, C. H. Shen, D. S. Shy, X. K. Xing, J.-F. Lee and J. M. Chen, *J. Phys. Chem. B*, 2008, **112**, 11250–11257.

22 K. L. Harrison and A. Manthiram, *Chem. Mater.*, 2013, **25**, 1751–1760.

23 K. L. Harrison, C. A. Bridges, M. P. Paranthaman, C. U. Segre, J. Katsoudas, V. A. Maroni, J. C. Idrobo, J. B. Goodenough and A. Manthiram, *Chem. Mater.*, 2013, **25**, 768–781.

24 F. Omenya, N. A. Chernova, S. Upreti, P. Y. Zavalij, K. W. Nam, X. Q. Yang and M. S. Whittingham, *Chem. Mater.*, 2011, **23**, 4733–4740.

25 F. Omenya, N. A. Chernova, Q. Wang, R. Zhang and M. S. Whittingham, *Chem. Mater.*, 2013, **25**, 2691–2699.

26 F. Omenya, N. A. Chernova, R. Zhang, J. Fang, Y. Huang, F. Cohen, N. Dobrzynski, S. Senanayake, W. Xu and M. S. Whittingham, *Chem. Mater.*, 2013, **25**, 85–89.

27 L. Xiong, Y. Wang, Y. Wu, W. Liu and Z. He, *Ionics (Kiel).*, 2015, **21**, 2471–2476.

28 M. A. Bustam, Z. Man, S. Maitra and T. Ishihara, *Trans. Indian Ceram. Soc.*, 2013, **72**, 108–112.

29 D. J. Park, R. Rajagopal and K. S. Ryu, *J. Ind. Eng. Chem.*, 2019, 1–11.

30 S. H. Lee and K. S. Ryu, *Bull. Korean Chem. Soc.*, 2018, **39**, 1266–1272.

31 A. V. Lavrov, V. P. Nikolaev, G. G. Sadikov and M. A. Porai-Koshits, *Sov. Phys. Dokl.*, 1982, **27**, 680.

32 J. Rana, Y. Shi, M. J. Zuba, K. M. Wiaderek, J. Feng, H. Zhou, J. Ding, T. Wu, G. Cibin, M. Balasubramanian, F. Omenya, N. A. Chernova, K. W. Chapman, M. S. Whittingham and L. F. J. Piper, *J. Mater. Chem. A*, 2018, **6**, 20669–20677.

33 V. V Guliants, J. B. Benziger, S. Sundaresan, I. E. Wachs, J.-M. Jehng and J. E. Roberts, *Catal. Today*, 1996, **28**, 275–295.

34 N. F. Quackenbush, L. Wangoh, D. O. Scanlon, R. Zhang, Y. Chung, Z. Chen, B. Wen, Y. Lin, J. C. Woicik, N. A. Chernova, S. P. Ong, M. S. Whittingham and L. F. J. Piper, *Chem. Mater.*, 2015, **27**, 8211–8219.

35 K. T. Jacob, S. Raj and L. Rannesh, *Zeitschrift fuer Met. Res. Adv. Tech.*, 2007, **98**, 776–779.

36 K. Lee, Personal Communication.